

## Microstructure and Corrosion behavior of Friction Stir-Welded AZ31 alloy

Yao Yao<sup>1,2</sup>, Jiaxin Tang<sup>1</sup>, Tianqi Chen<sup>1</sup>, Zhifeng Wang<sup>2</sup>, Hui Yu<sup>2</sup>, Changxing Zhou<sup>2</sup>,  
Hanqing Xiong<sup>1,2,3,\*</sup>

<sup>1</sup> Department of Mechanical and Electronic Engineering, Changsha University, Changsha 410022, China

<sup>2</sup> Hunan Joinfront Welding Technology Co., Ltd., Zhuzhou 412000, China

<sup>3</sup> School of Materials Science and Engineering, Hebei University of Technology, Tianjin 300130, China

\*E-mail: [xhanqing@163.com](mailto:xhanqing@163.com)

*Received:* 1 October 2019 / *Accepted:* 21 November 2019 / *Published:* 31 December 2019

---

Microstructure and corrosion behavior in stir zone (SZ), thermo-mechanically affected zone (TMAZ), heat affected zone (HAZ) and base material (BM) of friction stir welded (FSWed) AZ31 alloy are investigated in this study. Results indicate that the four zones show microstructure evolution due to localized heat and plastic deformation during FSW process. Electrochemical measurements and immersion test demonstrate that the TMAZ presents lower corrosion resistance because of non-uniform microstructure. Furthermore, the HAZ is influenced by heat flow leading to the stress release. Although the HAZ exhibits coarse grains, the distribution of grain size is relatively homogenous. Thus, the HAZ displays the low corrosion current density, the low corrosion rate and the high Impedance value, possesses better corrosion resistance.

---

**Keywords:** Mg alloy; Friction stir welding; Microstructure; Electrochemical property; Corrosion behavior

### 1. INTRODUCTION

Mg alloy, as a conspicuous structural material during the manufacture of aviation, spaceflight, automobile and electronic industries, provides the low density and high specific strength [1, 2]. Given the emission of greenhouse gas and the increase of fuel efficiency, Mg alloy has potential to be widely applied in various components and parts for the weight reduction [3]. Unfortunately, the poor deformation property has already become a strong factor hindering the development of Mg alloys due to specific crystal structure (HCP). Using the conventional fusion welding techniques to joint Mg alloys, porosity, oxide layer and brittle intermetallic compounds are favorite to form owing to a high chemical

activity [4, 5]. Friction stir welding (FSW) can be carried out at lower temperature to reduce the generation of intermetallic compounds in Mg alloy joints and improve the welding quality, which is regarded as an advanced welding technique with widely application in the vast manufacture fields [6]. However, inhomogeneous microstructure is produced in the welding process because temperature and strain gradient change has vital influence on material flow [7]. Furthermore, the process of stirring also induces strain localization and stress concentration in the welded nugget and the surrounding area seriously deteriorating mechanical and corrosion properties of welded Mg alloys [8-10]. Thus, the hidden safety problem of Mg alloy joints may be caused by FSW in the service course.

Currently, considerable researches are carried out on the improvement of the mechanical properties of FSWed Mg alloy joints. For a similar Mg alloy joint, the occurrence of localized corrosion is attributed to non-uniform microstructure as well as stress concentration [11]. At a dissimilar Mg alloy joint, a preferential corrosion occurs at the Mg alloy with lower corrosion potential, which also illuminates that the Mg alloy presents a higher corrosion rate in FSWed Al/Mg joints [12, 13]. Moreover, strength and fatigue life of Mg alloy joints are damaged with further corrosion [14]. For Mg alloys, this poor resistance seems to be entirely natural and thus relatively little attention has been paid to measurements of actual corrosion behavior which involves FSWed Mg alloy joints [15]. AZ series Mg alloys is the well-known in the structural applications. AZ31 alloy with 3% aluminum and 1% zinc exhibits better corrosion resistance because more  $Mg_{17}Al_{12}$  phase significantly influences corrosion properties of Mg alloys [16, 17]. During the welding operation, Mg alloy presents different microstructure evolution in stir zone (SZ), thermo-mechanically affected zone (TMAZ), heat affected zone (HAZ) and base material (BM). According to the research related to friction stir spot welding (FSSW), the increased dwell time and rotational speed accelerate the corrosion rate of AZ31 alloy [18]. Savguira [19] reported the microstructure variation and residual stress have a minor effect on corrosion resistance of FSSWed AZ31B joints. Considering the dissolution of intermetallics and the occurrence of dynamic recrystallization, the electrochemical behavior is changed in different regions, especially electrochemical potential [18, 20]. The stir zones in AZ31B spot and seam welds are nobler than the other regions. However, Aperador [21] found that the corrosion under stress is more appreciable for welded AZ31B using the FSW technique. The effect of microstructure evolution during the welding process on the corrosion behavior of the joint is still not fully understood. The differences in the electrochemical behavior of different regions are related to their microstructure evolution during the welding operation. Therefore, the investigation on the corrosion behavior of different regions contributes to improve the service performance of FSWed Mg alloys. In this study, the corrosion behavior in different regions of FSWed AZ31 alloy has been evaluated through microstructure observations, electrochemical measurements, mass loss test and examination of corrosion morphology.

## 2. EXPERIMENTAL

A commercial AZ31 Mg alloy was multi-pass hot rolled at 400°C to obtain 6 mm thick sheets. The chemical composition of the base material analyzed by inductively coupled plasma atomic emission spectrometry (ICP-AES, PS-6) is presented in the table 1. The work pieces were cut into designed size

100 × 300 × 6mm and then were friction stir welded on plate using two-dimensional moving gantry friction stir welding equipment in Joinfront Welding Technology Co. Ltd. Before the welding, the pieces were polished and cleaned to remove an oxide layer. Furthermore, it noted that the direction of welding perpendicular to the rolled direction. The tool was rotated in the counterclockwise direction at 1200 rpm and joints were made using a transverse speed of 100 mm/min, the tool was positioned at 2.5° tilt angle, the tool has a shoulder diameter of 17 mm, pin diameter of 6 mm.

**Table 1.** Chemical composition of rolled AZ31 alloy sheets.

Mg	Al	Zn	Mn	Fe	Cu	Ni	Si
Balance	2.8	0.7	0.25	<0.005	<0.005	<0.005	<0.005

Samples for microstructure observation were the cross-sections of the welds containing different welding regions. It used the low speed wire electrical discharge machine with cooling liquid to prevent microstructure changes in the weld zone. For optical microscopy and grain size measurement, samples were polished with 1200 grit abrasive paper and then etched using the etchant composed of 1 ml nitric acid, 1 ml acetic acid, 1 g oxalic acid, and 70 ml distilled water. Test samples were etched for varying time from 20s. An optical microscope (OM, XJP-6A) was used for microstructure observation, and the average grain size was evaluated by the linear intercept method [22]. The distribution of second phases in different regions was observed with a scanning electron microscope (SEM, Quanta-200) using backscattered electron (BSE) image. Micro-hardness of samples was measured using a hardness testing device (HXD-2000TMC/LCD) with the load of 1.96N for 10s.

Electrochemical properties of individual regions (SZ, TMAZ, HAZ and BM) in completed AZ31B joints were measured using an Adminal electrochemical workstation (Squidstat Plus) with a traditional three-electrode system. The counter electrode used a platinum sheet (4 × 4 × 0.2mm), and the reference electrode was silver chloride electrode (Ag/AgCl). The sample containing an individual region was employed as the working electrode. The sample was sealed with resin and only the cross-sectional surface of 0.6~0.8 cm<sup>2</sup> was exposed for electrochemical tests in 3.5% NaCl solution. It should be noted that the exposed surface of samples was measured due to individual regions with different sizes. Open circuit potential (OCP) was detected after samples were soaked in the electrolyte for 20 min. Potentiodynamic polarization curves were tested at the range of ± 300 mV around OCP with a scan rate of 1 mV s<sup>-1</sup>. Electrochemical impedance spectra (EIS) was tested at OCP with a 5 mV sine perturbation from 100 kHz to 0.01Hz.

Experimental specimens were immersed for 7 days to perform measurements of mass loss. The immersed sample also was sealed with the exposed cross-sectional surface. Before and after immersing test, the original weight ( $M_0$ ) and the final weight ( $M_1$ ) of samples were recorded respectively. In order to obtain  $M_1$ , the corrosion products on immersed samples were removed using a boiling solution of 100g/L chromic acid and 5g/L silver nitrate. The mass loss  $\Delta M$  was calculated using the following equation 1.

$$\Delta M = M_0 - M_1 \quad (1)$$

Furthermore, the corrosion rate of FSWed AZ31 with individual regions is evaluated using the equation 2.

$$\text{corrosion rate (mm/year)} = \frac{8.76 \times 10^4 \times \Delta M}{S \times \rho \times t} \quad (2)$$

Where S is the exposed surface area of an immersed specimen (cm<sup>2</sup>), ρ is the density of the experimental AZ31B alloy (roughly equal to 1.72g/cm<sup>3</sup>), and t is the immersed time (h).

### 3. RESULTS AND DISCUSSION

#### 3.1 Microstructure

The cross-sectional view of FSWed AZ31 alloy with different regions is shown in Fig. 1. Observably, stir zone (SZ), thermo-mechanically affected zone (TMAZ) and heat affected zone (HAZ) are included, and the centerline is marked in Fig.1. Microstructures of different regions can be further investigated with the increase of magnification in Fig.2a, b and c. Meanwhile, the original microstructure of base material (BM) is provided in Fig.2d. Lots of equiaxed grains are observed in the BM while fine dynamic recrystallized grains distribute in the direction of rolling. This non-uniform microstructure is induced through plastic deformation during hot rolling [23]. In the SZ (Fig. 3a), the microstructure is mainly comprised of dynamic recrystallized grains. Compared with the base material, the SZ exhibits more uniform microstructure in spite of the occurrence of dynamic recrystallization influenced by localized heat and plastic deformation during FSW process. Furthermore, the average grain size of 5-6μm in SZ, which is close agreement with previous observations [19]. The TMAZ is also affected by stirring force and localized heat considerably. The force from stir tool and shoulder makes metal flow to form the non-uniform microstructure in TMAZ, as shown in Fig. 3b. With the effect of thermal diffusion on the grain growth process, the TMAZ possesses larger grains than the SZ. The average grain size is the TMAZ is about 10-20μm. In Fig.3c, HAZ shows the microstructure with coarse grains similar to that in BM, but few fine dynamic recrystallized grains are observed because the HAZ is only influenced by heat flow. Thus, HAZ presents more uniform microstructure than that of BM.

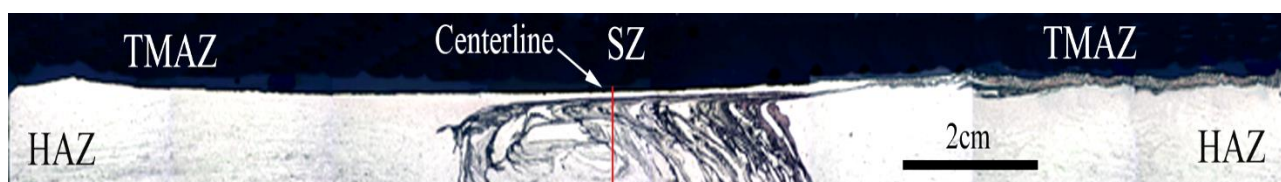


**Figure 1.** Cross-sectional view of FSWed AZ31 alloy, heat affected zone (HAZ), thermo mechanically affected zone (TMAZ) and stir zone (SZ).

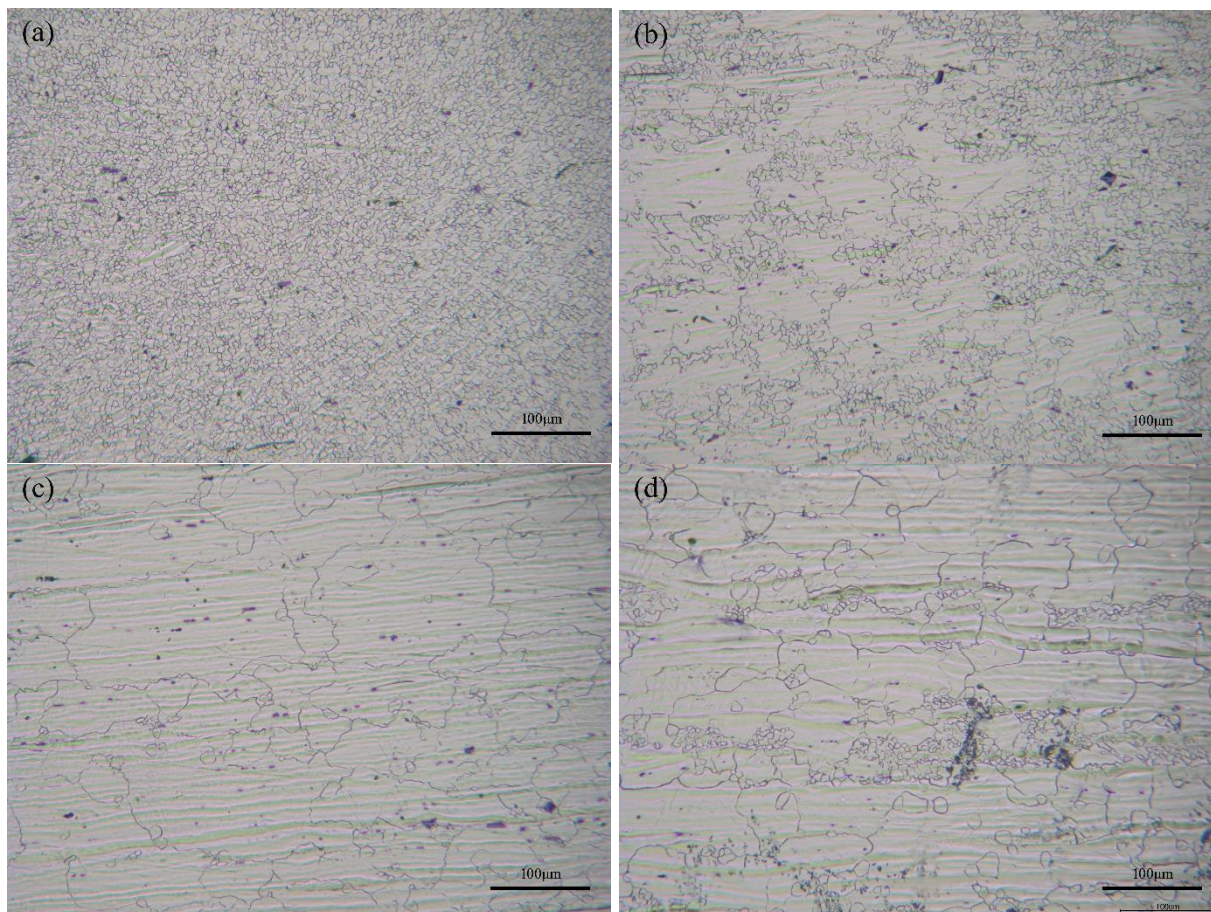


**Figure 2.** Optical micrographs of (a) SZ, (b) TMAZ, (c) HAZ and (d) BM of FSWed AZ31 alloy.

Fig. 3 shows BSE images of SZ, TMAZ, HAZ and BM. During FSW process, HAZ and BM do not experience a plastic deformation and, their initial microstructure is remained basically. Thus, it can be seen from Fig. 3c and d that white particles distribute along the rolling direction (RD), which is attributed to the great pressure during the hot rolling process. The white particle is further investigated by SEM and EDS maps in Fig. 4. The white particle is mainly composed of Al and Mn elements according to Fig. 4b. Considering the low content of Mn, Al-Mn intermetallics are not recognized and, it may be  $Al_8Mn_5$  or  $Al_6Mn$  [24, 25]. Fig. 4b also confirmed that Zn element exists in  $\alpha$ -Mg matrix in the form of solid solution, because the EDS element map indicates that Zn element exhibits the homogeneous distribution. Additionally, Zn element possesses a relatively high solid solubility in Mg-Zn alloy and there is a little Zn in experimental alloy. With the force from stir tool and shoulder during FSW process, Al-Mn intermetallics are crushed and broken down into tiny particles discretely in SZ and TMAZ. Additionally, the experimental AZ31 is thicker than that of previous reports [19, 26]. The temperature during friction stir welding is lower than the melting temperature of Al-Mn intermetallics [9, 25]. Thus, Al-Mn intermetallics are remained in  $\alpha$ -Mg matrix and lots of fine dispersed Al-Mn intermetallics are observed in Fig. 3a and b.

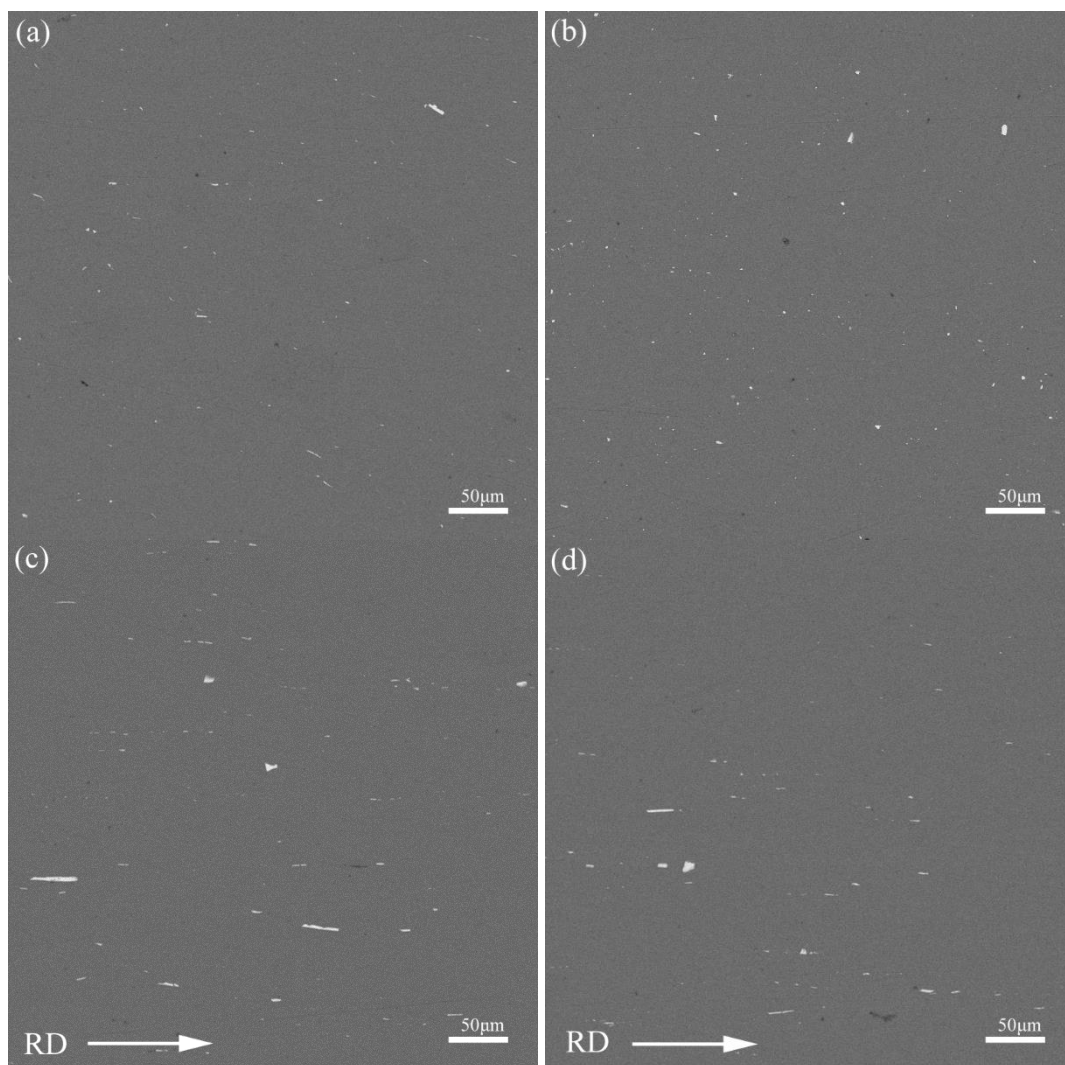


**Figure 3.** BSE images of (a) HAZ, (b) TMAZ (c) SZ and (a) BM of FSWed AZ31 alloy.

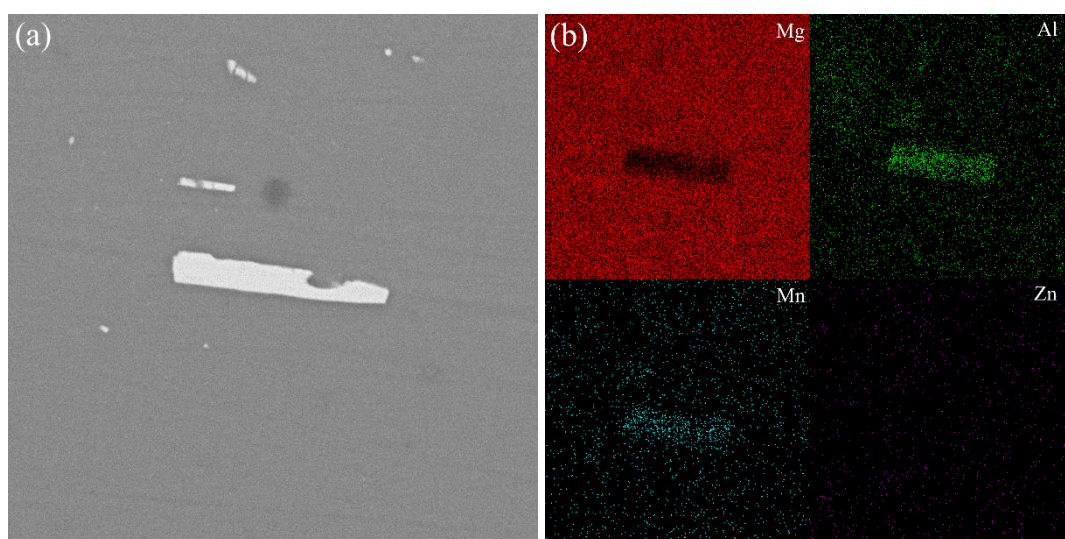


**Figure 4.** Morphology (a) and EDS map (b) of second phase.

### 3.2 Micro-hardness test

In order to further evaluate the difference in individual regions of FSWed AZ31 alloy, micro-hardness values on cross-sectional surface are measured and shown in Fig.4. Generally, the SZ can be easily distinguished due to a significant change in micro-hardness values. The SZ exhibits higher micro-hardness values relative to the BM because of fine grains produced by the FSW process. The highest micro-hardness occurs at this location, since metal immediately suffers stir and compressive deformation to form fine grains. In addition, the dislocation density can be also contribution to the increase in micro-hardness. Although a substantial portion of dislocations is removed with local temperatures during the FSW process, retained dislocations have more or less effect on the residual stress and the micro-hardness [26, 27]. The micro-hardness in the TMAZ is also depended on plastic deformation and heat flow during the FSW process. The local plastic deformation improves the micro-hardness value due to the increase in dislocation density, and the thermal diffusion promotes a partial recrystallization in the zone leading to dislocation motion and material softening. The HAZ shows lower micro-hardness values than those of the other zone. The lowest micro-hardness value were found close to the TMAZ/HAZ boundary, and then the HAZ presents gradually the increased micro-hardness value with the increase of distance from welding centerline. This is consistent with recrystallization and grain growth affected by the local temperatures during the FSW process. The temperature decreases with the increase of distance, the degree of recrystallization and grain growth decreases. When the distance increases to a certain limit, the thermal energy input cannot induce the occurrence of recrystallization. The micro-hardness value is close to the original one of BM.

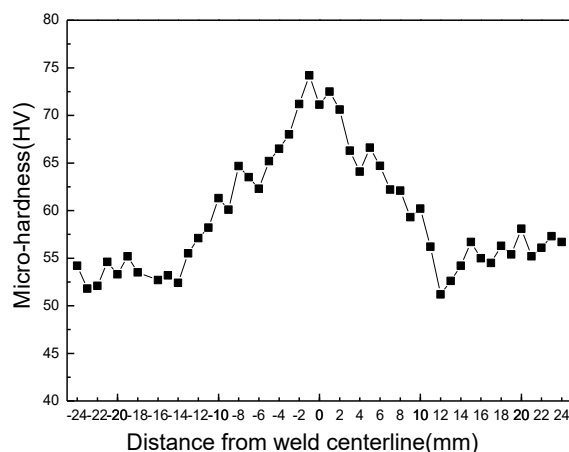


**Figure 5.** Micro-hardness values on cross-sectional surface of FSWed AZ31 alloy.

### 3.3 Corrosion property

#### 3.3.1. Open Circuit Potential

Fig.6 shows Open Circuit Potential (OCP)-time curves of every individual region in 3.5% NaCl solution. The electrochemical state on the surface of tested specimens can be reflected by OCP curves,

since some information can be used to evaluate the origin and propagation of corrosion [28]. After a short time, the relatively stable OCP values are presented in Fig. 6. Moreover, it can be seen that the OCP values of different regions increase in the following order: SZ < THAZ < BM < HAZ. To a certain extent, the steady values represent the electrochemical activity of different tested regions. Observably, the change of OCP values is related to the microstructure in different regions, which implies different driving forces of corrosion in different regions. For the SZ, the average grain size is smaller than other zones, which results in the increasing grain boundaries. The increased boundaries can provide more electrochemical reaction channels improving the driving force of corrosion [29, 30]. The average grain size exhibited in Fig. 2 also is ranked as SZ < THAZ < BM < HAZ. Additionally, the Al-Mn phase is the strong local cathode to promote the hydrogen evolution and local corrosion [31]. Thus, the distribution and the size of second phases in Fig. 3 also cause to the change in driving force of corrosion. The relatively small Al-Mn phases can provide the initiation of corrosion in SZ and THAZ, which makes the OCP towards the negative direction.

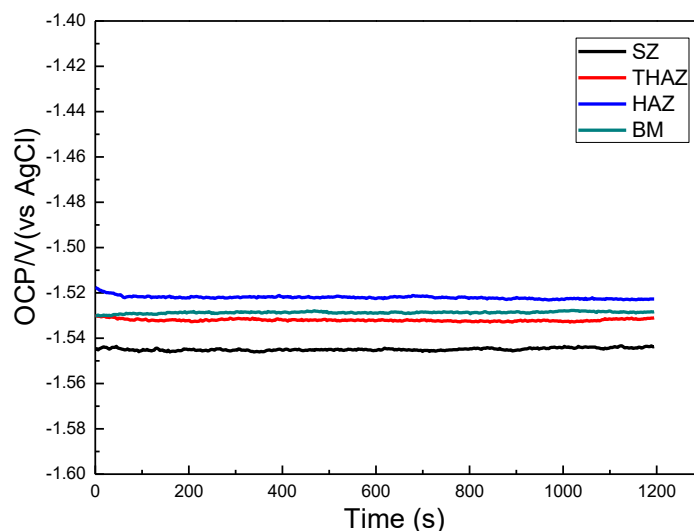


**Figure 6.** Open Circuit Potential-time curves of isolated zones from FSWed AZ31 alloy in 3.5% NaCl solution.

### 3.3.2 Potentiodynamic polarization measurements

In Fig. 7, corrosion performance of specimens included every individual region is investigated in 3.5% NaCl solution using potentiodynamic polarization measurement. Then, the related corrosion parameters are listed in Table 2. The corrosion potential ( $E_{\text{corr}}$ ) values of different regions are ranked as the similar order to OCP values apparently. Actually, the  $E_{\text{corr}}$  is employed to evaluate the electrochemical activity of experimental alloys [32]. It can be seen from Fig.7 and Table 2 that the driving force of corrosion in different regions is different. Moreover, the similar asymmetrical structure is found on polarization curves of different regions, without passivation stage over the testing range. The relation between microstructure and corrosion behavior of different tested regions can be revealed by

the related polarization curves. The anodic branch represents the dissolution of magnesium according to the formula (3). For four different regions, the anodic currents increase rapidly with potential variation because of the negative difference effect [33]. Furthermore, the corrosion current ( $j_{\text{corr}}$ ) is hard to be extrapolated through the anodic branch of the polarization curve due to the indistinct Tafel region. Thus, the  $j_{\text{corr}}$  values are only evaluated by the cathodic branch considering the hydrogen evolution the reaction 4 [34].



Table 2 shows the  $j_{\text{corr}}$  values of different regions increasing in following order: HAZ < BM < SZ < THAZ. The THAZ is comprised of non-uniform grains and fine Al-Mn particles so as to exhibit the larger  $j_{\text{corr}}$  value than other zones. Compared with the THAZ, the SZ possesses smaller and more uniform grains [11].

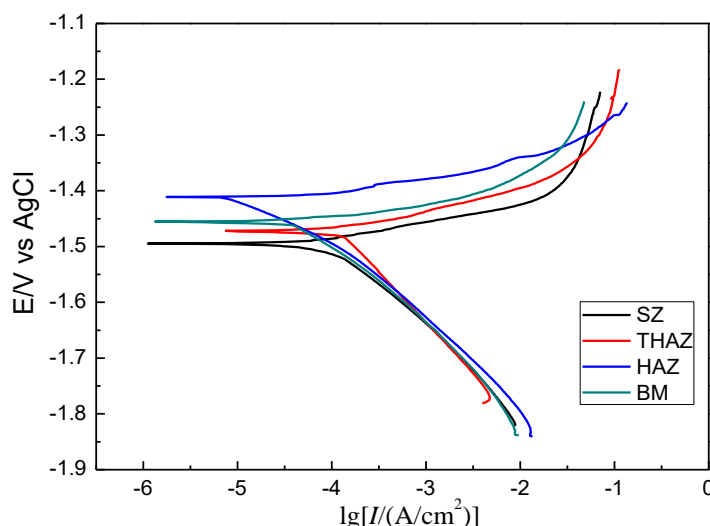


**Figure 7.** Potentiodynamic polarization curves of isolated zones from FSWed AZ31 alloy in 3.5% NaCl solution with a scan rate of 1 mV s<sup>-1</sup>.

**Table 2.** Polarization curve fitting data of individual regions from FSWed AZ31 alloy in 3.5% NaCl solution with a scan rate of 1 mV s<sup>-1</sup>.

Region	$E_{\text{corr}}/\text{V}(\text{vs SCE})$	$j_{\text{corr}}/(\mu\text{A}\cdot\text{cm}^2)$
SZ	-1.494	47.8
TMAZ	-1.471	82.9
HAZ	-1.455	8.32
BM	-1.411	27.5

Although fine Al-Mn particles also remained in the SZ, the uniform and fine grains are favorable to the improvement of corrosion resistance [35]. In the same way, the grain size of the HAZ is larger

than that of the BM, but the HAZ shows the smaller  $j_{\text{corr}}$  value which is mainly attributed to the uniform grain structure, as shown in Fig. 2. Actually, the uniform grain structure in the HAZ is partly dependent on the effect of heat flow during FSW process, which induces the growth of fine dynamic recrystallization and stress release. The high dislocation density is a contribution to the increase of stress and hardness [27]. On the contrary, the rise of micro-hardness in the SZ is determined by both grain refinement and high dislocation density, as shown in Fig. 5. Thus, the SZ presents lower corrosion resistance compared with BM and HAZ because of crystalline defects caused by abundant dislocations and high deformation energy [36].

### 3.3.3 Electrochemical impedance spectra (EIS)

Fig.8 gives EIS plots of four different regions and the equivalent circuit. Observably, specimens for different regions exhibit similar plots which are comprised of a big loop and a small loop, and thus the corresponding equivalent circuit is shown in the insert image. Table 3 lists the fitting data according to the equivalent circuit. Where,  $R_s$  represents the solution resistance depended on the electrolyte concentration,  $R_t$  is charge transfer resistance and  $R_f$  reflects effects of corroded film. It should be noted that the double-layer capacitance (C) is replaced by the constant phase element (CPE) for a precious fitting data, as the following equation 5 [37].

$$Z(j\omega) = (Y_0)^{-1}(j\omega)^{-n} \quad (5)$$

Where,  $Y_0$  is regarded as the CPE-constant, and the imaginary unit is expressed by  $j$ . The angular frequency ( $\omega$ ) is related to the frequency ( $f$ ), the regular expression is  $\omega = 2\pi f$ , and  $n$  is the power ( $0 < n \leq 1$ ). If  $n$  is 1, CPE means a pure capacitance. For the equation, the change of  $n$  is determined by the heterogeneous effect.  $CPE_1$  reflects the double-layer capacitance implying the charge-transfer on the interface between the electrolyte and the electrode, and moreover  $CPE_2$  is the capacity of corroded film due to the charge-transfer and the ion-diffusion [38, 39]. Therefore, the polarization resistance ( $R_p$ ) can be defined as the following equation 6.

$$R_p = R_t + R_f \quad (6)$$

Since the exchange current is directly associated with the self-corrosion, the  $R_p$  is used to evaluate the corrosion resistance of different regions.  $R_p$  values are also ranked as  $HAZ < BM < SZ < THAZ$ , which is in agreement with the result of potentiodynamic polarization measurement.

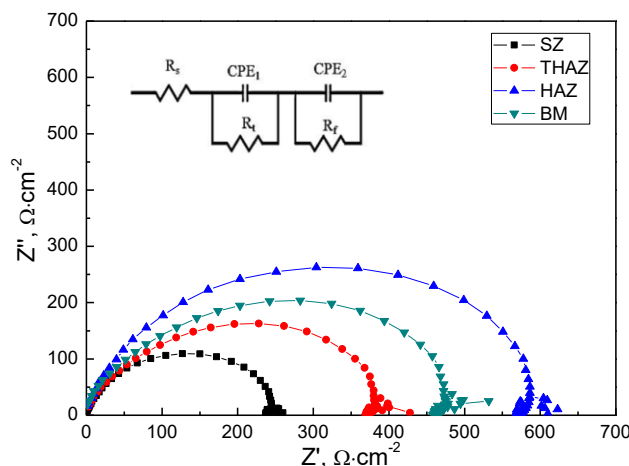


**Figure 8.** EIS plots of individual regions from FSWed AZ31 alloy in 3.5% NaCl

**Table 3.** EIS simulated values of individual regions from FSWed AZ31 alloy in 3.5% NaCl

Region	SZ1	TMAZ3	HAZ	BM2
$R_s (\Omega \cdot \text{cm}^2)$	1.025	2.867	1.084	2.5502
$CPE_1 (\Omega^{-1} \cdot \text{cm}^{-2} \cdot \text{s}^n)$	$4.808 \times 10^{-7}$	$3.018 \times 10^{-7}$	$2.021 \times 10^{-7}$	$5.858 \times 10^{-7}$
$n_1 (0 < n < 1)$	1	0.9255	0.9989	1
$R_t (\Omega \cdot \text{cm}^2)$	190.7	380.4	570.5	460.3
$CPE_2 (\Omega^{-1} \cdot \text{cm}^{-2} \cdot \text{s}^n)$	$1.38 \times 10^{-6}$	0.001802	$9.241 \times 10^{-7}$	$2.325 \times 10^{-7}$
$n_2 (0 < n < 1)$	0.8812	0.7853	0.7621	0.897
$R_f (\Omega \cdot \text{cm}^2)$	54.29	99.7	63.2	69.1
$\chi^2$	$5.53 \times 10^{-4}$	$8.12 \times 10^{-4}$	$3.09 \times 10^{-3}$	$5.42 \times 10^{-4}$

### 3.3.4 Immersion test

Fig.9 shows typical morphologies of the specimens in different regions after different intervals of immersion in 3.5% NaCl solution. When the immersion time is 25min, the THAZ obviously exhibits more initiation sites for pitting corrosion than other regions. As the immersion time is increased from 25 to 50 min and further 100 min, the extent of erosion in different regions is aggravated. For specimens in THAZ and SZ, the surface is entirely corroded. For specimens in HAZ and BM, it can observe parts of uncorrupted surface. Compared with other regions, the THAZ presents severe corrosion. In Fig. 10, the corroded morphology observed by SEM shows the initiation sites for pitting corrosion are related to Al-Mn particles with strong cathode effect. After 7 days of immersion in 3.5 wt.% NaCl solution, the corrosion rates of the specimens in different regions calculated from the weight loss measurements are shown in Fig. 11. The result also means that the THAZ possesses the faster corrosion rate, which is in good agreement with polarization test and EIS results.

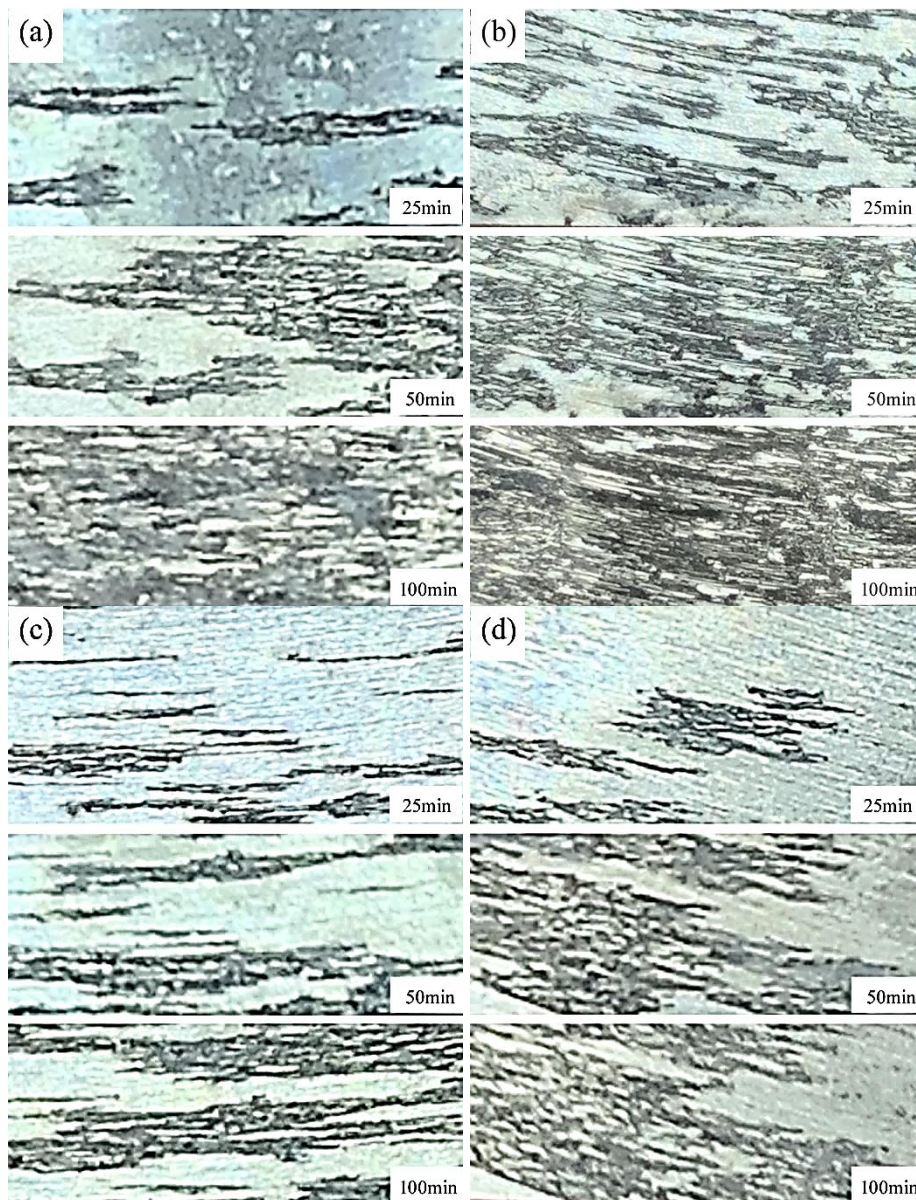


**Figure 9.** Typical corrosion morphologies of the isolated (a) SZ, (b) THAZ, (c) HAZ and (d) BM after different intervals of immersion in 3.5% NaCl solution.

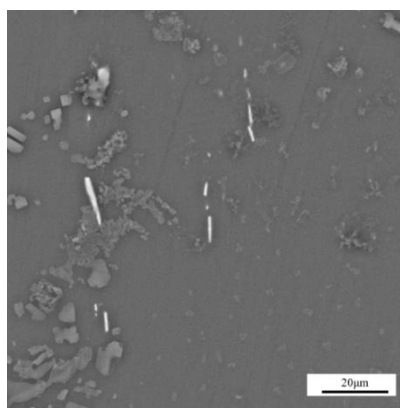


**Figure 10.** The corroded morphology of THAZ after immersion for 25min in 3.5 wt.% NaCl solution.

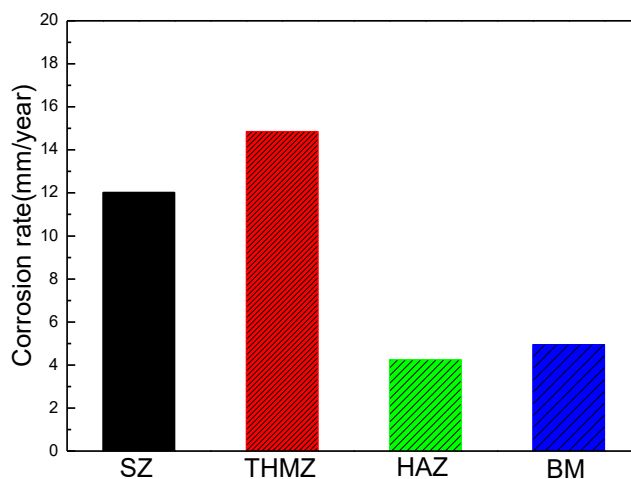


**Figure 11.** Corrosion rate of the specimens in different regions evaluated after 7 days of immersion in 3.5 wt.% NaCl solution .

#### 4. CONCLUSIONS

Hot rolled AZ31 plates were friction stir welded in this work. Microstructure and corrosion behavior of different regions in FSWed AZ31 alloy were investigated by microstructure observation, electrochemical measurement and immersion test. It has been found that the stir zone exhibits uniform and fine equiaxed grains influenced by localized heat and plastic deformation during FSW process, the thermo-mechanically affected zone possesses coarse and fine grain structure, while heat affected zone shows the microstructure with coarse grains similar to that in base material. The thermo-mechanically affected zone presents lower corrosion resistance, while heat affected zone possesses better corrosion resistance due to the uniform microstructure.

#### ACKNOWLEDGEMENT

This work was financially supported by the Fundamental Research Funds for the Education Department of Hunan Province (17A019), China. The authors also acknowledge the Project (KC1809018, K1705051) supported by the science and technology program of Changsha and the outstanding youth project (18B418) of Education Department of Hunan Province, China.

#### References

1. X. Zhang, Y. Chen, J. Hu, *Prog. in Aerosp. Sci.*, 97 (2018) 22.
2. X. J. Wang, D. K. Xu, R. Z. Wu, *J. Mater. Sci. Technol.*, 34 (2018) 245.
3. A. A. Luo, *J. Magnes. Alloys*, 1 (2013) 2.
4. Y. Chen, C. He, K. Yang, *Int. J. Fatigue*, 122 (2019) 218.
5. R. Z. Xu, D. R. Ni, Q. Yang, *J. Mater. Sci. Technol.*, 32 (2016) 76.
6. V. M. Magalhães, C. Leitão, D. M. Rodrigues, *Sci. Technol. Weld. Joi.*, 23 (2018) 400.
7. S. Mironov, Y. S. Sato, H. Kokawa, *Metall. Mater. Trans. A*, 50 (2019) 2798.
8. Q. Liu, Q. Ma, G. Chen, *Corros. Sci.*, 138 (2018) 284.
9. Y. Savguira, T. H. North, A. P. Gerlich, *J. Electrochem. Soc.*, 165 (2018) C794.

10. G. Liu, Z. Ma, G. Wei, *J. Mater. Process. Tech.*, 267 (2019) 393.
11. A. James, T. H. North, S. J. Thorpe, *ECS Trans.*, 41 (2012) 193.
12. Savguira Y, T. H. North, S. J. Thorpe, *J. Electrochem. Soc.*, 165 (2018) C1.
13. B. Ratna Sunil, G. Pradeep Kumar Reddy, *Cogent Engineering*, 3 (2016) 1145565.
14. S. Mironov, T. Onuma, Y. S. Sato, *Mater. Sci. Eng. A*, 679 (2017) 272.
15. H. Liu, F. Cao, G. Song, *J. Mater. Sci. Technol.*, 35 (2019) 2003.
16. J. Tkacz, K. Slouková, J. Minda, *Metals*, 7 (2017) 465.
17. S. Mironov, T. Onuma, Y. S. Sato, *Acta Mater.*, 100 (2015) 301.
18. Y. Savguira, W. H. Liu, D. J. Miklas, *Corrosion*, 7(2014) 858.
19. Y. Savguira, T. H. North, S. J. Thorpe, *Mater. Corros.*, 67 (2016) 1068.
20. Q. Liu, Q. Ma, G. Chen, *Corros. Sci.*, 138 (2018) 284.
21. W. Aperador, J. Cortes, A. Delgado, *Int. J. Electrochem. Sci.*, 8 (2013) 12487.
22. E112-10, ASTM International, West Conshohocken, PA,(2010), DOI: 10.1520/E0112-10
23. H. Zhu, H. Liu, Fang H, *Int. J. Electrochem. Sci.*, 13 (2018) 11180.
24. G. B. Hamu, D. Eliezer, L. Wagner, *J. Alloy Comp.*, 468 (2009) 222.
25. X. J. Liu, I. Ohnuma, R. Kainuma, *J. Phase Equilib.*, 20 (1999) 45.
26. J. R. Kish, G. Williams, J. R. McDermid, *J. Electrochem. Soc.*, 161 (2014) C405.
27. J. A. Esparza, W. C. Davis, E. A. Trillo, *J. Mater. Sci. Lett.*, 21 (2002) 917.
28. J. Li, K. Wan, Q. Jiang, *Metals*, 6 (2016) 65.
29. L. Fan, H. Lu, J. Leng, *Electrochim. Acta*, 165 (2015) 22.
30. H. Xiong, L. Li, Y. Zhang, *J. Electrochem. Soc.*, 164 (2017) A1745.
31. N. G. Wang, R. C. Wang, C. Q. Peng, *Corrosion*, 68 (2012) 388.
32. Y. Wu, Z. Wang, Y. Liu, *Int. J. Electrochem. Sci.*, 13 (2018) 10325.
33. G. Song, A. Atrens, M. Dargusch, *Corros. Sci.*, 41 (1998) 2493.
34. L. G. Bland, A. D. King, N. Birbilis, *Corrosion*, 71(2014) 128.
35. H. Xiong, K. Yu, X. Yin, *J. Alloy Comp.*, 708 (2017) 652.
36. D. Song, A. Ma, J. Jiang, *Corros. Sci.*, 52 (2010) 481.
37. J. MA, J. Wen, G.X. Li, *Corros. Sci.*, 52 (2010) 534.
38. R. Udhayan, D. P. Bhatt, *J. power sources*, 63 (1996) 103.
39. T. Hong, Y. H. Sun, W. P. Jepson, *Corros. Sci.*, 44 (2002) 101.

© 2020 The Authors. Published by ESG ([www.electrochemsci.org](http://www.electrochemsci.org)). This article is an open access article distributed under the terms and conditions of the Creative Commons Attribution license (<http://creativecommons.org/licenses/by/4.0/>).